



Study of ZnO room temperature NO₂ sensor under illumination prepared by auto-combustion

M. Benamara¹ · S. Soreto Teixeira² · M. P. F. Graça² · M. A. Valente² · Suresh Kumar Jakka² · H. Dahman¹ · E. Dhahri³ · L. El Mir¹ · M. Debliquy⁴ · D. Lahem⁵

Received: 29 June 2021 / Accepted: 13 August 2021

© The Author(s), under exclusive licence to Springer-Verlag GmbH, DE part of Springer Nature 2021

Abstract

ZnO nanoparticles have been prepared by auto-combustion method. Morphological and structural properties of the prepared samples were investigated by SEM, XRD, Raman and XPS characterizations. The XRD diffractogram of the sample indicates that ZnO has a hexagonal wurtzite structure. The crystallites average size, calculated from the Williamson–Hall plot, was 69.3 nm and the estimated by the SEM image (76.86 nm). Raman investigation indicates different modes of atomic displacement which correspond to longitudinal/transversal optical components with different frequencies. These modes are due to the macroscopic electric fields associated with the basic phonon of hexagonal ZnO. The XPS spectra indicate the presence of Zn and O in the structure with a small number of interstitial Zn²⁺, oxygen vacancies (V_O), and a negligible amount of chemical bonds with carbon (=CO ...), confirmed by FTIR spectroscopy. The UV absorbance and reflectance spectra show a high absorbance with gap energy of 3.17 eV, estimated by Tauc's model. The a.c. electrical spectroscopy can be described by the Jonscher universal power-law. The charge carriers move according to the correlated barrier hopping pattern over the dispersive region. At room temperature, the conductivity of ZnO is high ($\sim 8 \times 10^{-6} \text{ S.m}^{-1}$) making it promises for gas detection applications. The sensor was prepared by spraying the suspension of ZnO nanopowders on alumina substrates with pre-deposited gold interdigitated electrodes. The sensor responses of NO₂, for concentrations of 0.5, 0.75 and 1 ppm, were investigated at room temperature under illumination with different wavelengths. The best response of the sensor was obtained for a concentration of 1 ppm NO₂ excited by 400 nm (purple) and 380 nm (UV) wavelengths, which were 91 and 88 with response/recovery times equal to 4/6.7 min and 4.4/3.3 min. Higher responses at the lower wavelength are due to the higher excitation energy which tends to excite more electrons, at the material surface, subsequently participating in the detection mechanism with gas molecules

Keywords Auto-combustion method · Room temperature gas sensor · NO₂ sensor · UV or visible light effect · Electrical properties

1 Introduction

Air pollution is a major global environmental risk to our health and food security. NO₂ is one of the polluting gases harmful to the human respiratory system, causing respiratory diseases as pulmonary edema, being also toxic for the environment since it is the main source of nitric acid responsible for acid rain [1, 2]. So, it is urgent to build low-cost sensors for rapid and efficient detection of toxic and dangerous gases, such as NO₂, and sensitive to low concentration. In recent years, metal oxide gas sensors attracted the attention of researchers due to their numerous useful features such as low concentration detection limit, high sensitivity,

✉ S. Soreto Teixeira
silvia.soreto@ua.pt

¹ Laboratory of Physics of Materials and Nanomaterials Applied At Environment (LaPhyMNE), Faculty of Sciences in Gabes, Gabes University, 6072 Gabes, Tunisia

² i3N and Physics Department, University of Aveiro, Campus Universitário de Santiago, 3810-193 Aveiro, Portugal

³ Laboratoire de Physique Appliquée, Faculté Des Sciences, Université de Sfax, B. P. 1171, 3000 Sfax, Tunisia

⁴ Service de Sciences Des Matériaux, Université de Mons, Rue de l'Épargne 56, 7000 Mons, Belgium

⁵ Materials R&D Center, Materia Nova, Parc Initialis, Avenue Nicolas Copernic 3, 7000 Mons, Belgium

good chemical and physical properties, low cost and high availability [3–5].

The sensing mechanism is based on the exchange of electrons between the surface of the material and the adsorbed gas molecules. Indeed, when a gas adsorbs on the surface, if the interaction is strong enough (chemisorption), an electron can take place, and the concentration of charge carriers in the semiconductor is affected. This surface doping is reversible. The conductivity change is directly related to the gas adsorption thanks to the adsorption equilibrium. The sensor consists of a pair of electrodes on an insulating substrate covered with a sensitive semiconductor. The useful signal is the resistance or impedance change between the electrodes. The choice of the sensitive materials depends on the target gas. The sensitive layer should be porous and present a high specific surface area to optimize the contact with the gas and the surface-to-volume ratio.

Traditional semiconductor gas sensors based on metal oxides must operate at high temperatures, to improve the detection kinetics which are too slow at room temperature. The ZnO-based sensors often operate at temperatures ranging from 200 to 600 °C [6, 7], which increases the energy consumption, the difficulty in choosing and designing the substrate and the manufacturing cost. High temperatures can induce grain growth and deteriorate long-term performance, which justifies the challenge of reducing the operating temperature of the sensors. The development of advanced nanostructured materials can reduce the working temperature of metal oxide-based gas sensors until reaching room temperature [8]. The synthesis and optimization of nanostructured metal oxides can be carried out in different ways, but the specific surface area should always be the key parameter. This is the main reason why a great effort has been made to synthesize nanomaterials, with one or two dimensions, with high specific surface area for gas detection applications.

NO₂ is an electron acceptor. As the sensing mechanism is based on the exchange of electrons between the surface of the material and the adsorbed gas molecules, there should be enough free electrons in the conduction band (CB) of the material to be captured by NO₂. However, in the case of broadband semiconductors, there are almost no free electrons in the conduction band at room temperature under dark conditions. The use of light irradiation is an effective strategy to reduce the operating temperature of broadband semiconductors as gas sensors. Therefore, lighting, instead of heating, can provide external energy to improve the response kinetics and increase the concentration of free electrons in the conduction band of semiconductors [9]. Recently, gas sensors based on ultraviolet (UV) activated metal oxide semiconductors have been reported [10–12]. Illuminating these sensors with UV light is an alternative to improve chemical reactions on the surface of the metal oxide without the need for heating [13, 14]. It has been suggested that ultraviolet

or visible light affects the performance of the gas sensor because it can facilitate the dissociation of gas and chemical components adsorbed on the surface [11, 12], increase the density of free electron–hole pairs and consequently creating electric carriers [15]. These physicochemical phenomena allow the detection of gas at room temperature and the use of these metal oxides as sensors activated by light for different applications with low energy consumption. The main differences between these two light sources are that the sources in the ultraviolet wavelength are expensive and consume energy, and the visible light sources are cheaper and more energy efficient. Therefore, visible light is a potential candidate to replace UV light to activate metal oxide gas sensors at room temperature [16]. Generally, electron–hole pairs are photo-generated only when the semiconductors are illuminated under light with photonic energy greater than its bandgap energy [17]. That is, for ZnO-based gas sensors the wavelength of the excitation light must be less than the wavelength corresponding to the intrinsic energy of the bandgap of ZnO [18, 19]. However, it has been shown that it is possible to work with longer wavelengths (smaller energy) because the physicochemical reactions on the surface demand less energy [16].

In this work, zinc oxide nanoparticles were prepared by the auto-combustion technique. Morphological and structural properties of the prepared sample were studied by Scanning Electron Microscopy (SEM), X-Ray Diffraction (XRD), X-ray photoelectron (XPS) and Raman spectroscopies. The optical properties of the prepared ZnO nanoparticles were investigated by UV–Vis–NIR and FTIR spectroscopies. The electrical characterization was carried out at several temperatures (200–400 K), in the frequency range of 100 Hz–1 MHz. The sensor was elaborated by spraying an aqueous solution of ZnO on an alumina substrate with gold interdigitated electrodes. The sensing properties of ZnO for a concentration 0.5, 0.75 and 1 ppm of NO₂ gas have been investigated. ZnO-based sensors were tested under different light illumination such as UV, purple, blue and green lights at room temperature. Strong responses were observed, especially under excitation with short light wavelengths.

2 Experimental details

2.1 Synthesis

Zinc oxide was prepared by the auto-combustion method. Dehydrated zinc acetate [Zn(CH₃COO)₂·2H₂O; 99%; Sigma Aldrich MFCD00066961] and glycine (NH₂CH₂COOH; Sigma Aldrich MFCD00008131) with a ratio (1:2), were dissolved in distilled water at room temperature. Glycine plays the role of fuel. The obtained solution was evaporated using a hot plate at 80 °C with constant magnetic stirring

until the formation of a viscous gel. This gel was ignited by raising the temperature up to 300 °C. The burnt powder was calcined in a muffle furnace at 600 °C for 7 h to remove the organic compounds with Carbone. The obtained nanopowders were ground manually for one hour.

2.2 Characterization

The structure, morphology and optical properties of the prepared sample were characterized by XRD, XPS, FE-SEM, UV–Vis-NIR spectroscopy, by Raman and FTIR spectroscopies. The microstructure of the prepared ZnO powders was carried out by an X-ray diffractometer (D8 Advance, Bruker AXS) and X-ray photoelectron spectroscopy (ESCALAB 250Xi, Thermo Scientific). XPS was recorded using AlK α , as a source with $h\nu = 1486.6$ eV under a vacuum of about 2×10^{-6} Pa. The XPS was calibrated using sputtered references material Ag (for peak position, work function), Au and Cu (for retard linearity). Charge compensation was done using dual compensation (electron and very low energy ion gun (Ar)). Charge compensation was checked using a reference PET sample. The morphological structure was obtained by field-emission scanning electron microscopy (S4800II, Hitachi). The optical properties were taken using UV–Vis-NIR spectrophotometer (Shimadzu UV-3101PC) in the wavelength range of 200 to 1800 nm and FTIR spectrophotometer. The Raman spectroscopy was performed by using a Jobin–Yvon spectrometer, at room temperature, in backscattering geometry with exciting light ($\lambda = 532$ nm).

The impedance spectroscopy technique, carried out in function of the sample temperature (200–400 K) and frequency of the applied ac field (100 Hz–1 MHz), was used with an *Agilent 4294* analyzer working with an amplitude of 500 mV. To perform this study, sample powders were pressed into pellets (diameter \approx 6 mm; thickness < 1 mm). The sample's electrodes were made by painting the opposite surfaces of the pellets with silver conductive paste. The measurements were performed in a helium atmosphere to improve the heat transfer and avoid moisture.

2.3 Sensing tests

With a probe-type Ultra sonicator 250 mg of the prepared ZnO nanopowder were dispersed in 2.25 ml of distilled water until a uniform solution were obtained. The prepared solution was deposited by spraying on interdigitated gold electrodes on alumina substrates (Al₂O₃) (C-MAC Micro Technology Company, Belgium) heated by a hot plate at 200 °C. To stabilize the deposited layer, the fabricated sensor was heat-treated at 400 °C, for 1 h.

The responses of ZnO-based sensors were studied at room temperature when submitted to light with different wavelengths. For the sensing tests, the electrical resistance was

measured when the sensor is in the air or in a gas atmosphere (NO₂). Figure 1 presents the scheme of the test chamber. Commercial Ultra-Violet, purple, blue and green LED lamps were used as the external photon source (Fig. 1 led bulb), fixed in a Teflon chamber, which is in front of the sensor under test. The light intensity was 3 mW/cm². The target gas concentration and zero air flow rate controlled by mass flow meters (El-flow, Bronkhorst). Before doing the sensing test synthetic air, 79% N₂ + 21% O₂ was injected into the cell, at a pressure of 1 atm, and the system was allowed to stabilize for approximately 2 h, until the electrical resistance was stable. Then NO₂ gas, with the desired concentration of 0.5, 0.75 and 1 ppm, was introduced in the test chamber, for a maximum of 15 min. The tests were performed in 50% relative humidity. For this half of the synthetic air is passed through a bubbler containing distilled water, at a temperature of 22 °C, before injection into the cell. The sensor result was defined by “Response = (R_{NO₂} - R_{air})/R_{air}”, where R_{NO₂} and R_{air} are the measured electrical resistance of the sensor in NO₂ gas and in the air, respectively. The response and recovery times were calculated at 90% of the resistance change after exposure to the target gas and air, respectively. The resistance was measured at the terminal of the two interdigitated electrodes covered with the deposited material.

3 Results and discussion.

3.1 Structural and morphological proprieties

The XRD diffractogram was refined (Fig. 2) using the Fullprof software [25]. The XRD peaks at $2\theta = 31.78^\circ$, 34.44° , 36.28° , 47.56° , 56.61° , 62.91° , 66.39° , 67.97° and 69.14° can be ascribed to the reticular plane of (100), (002), (101), (102), (110), (103), (200), (112) and (201), respectively, of the hexagonal structure of ZnO according to JCPDS No.

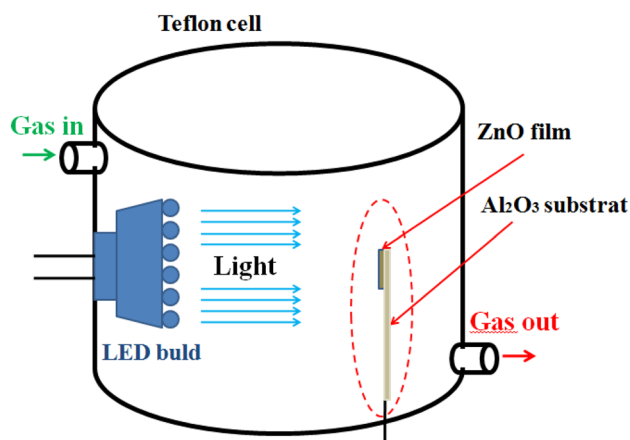


Fig. 1 Scheme of test chamber

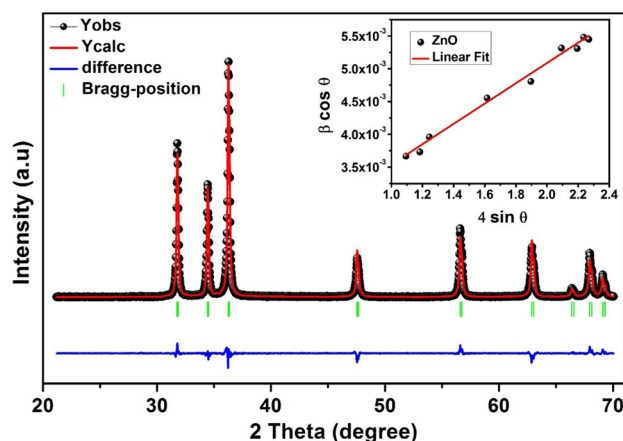


Fig. 2 Rietveld refinement of the X-ray diffraction pattern and Williamson–Hall plot for ZnO prepared by auto-combustion method

01-073-8765. The goodness of fit (χ^2) has a value closer to 1 (1.81) suggesting that the quality of the sample refinement is good. The average size of the crystallites and the deformation of the ZnO lattice were evaluated using the Williamson–Hall model expressed as follows: [20]

$$\beta \cos \theta = \frac{K\lambda}{D_{W-H}} + 4\varepsilon \sin \theta$$

where β and θ are the full width at half maximum and the angle of the diffraction peak, of the different planes (hkl). K is the shape factor (0.9), λ present the X-ray wavelength (0.154 nm), and ε is the lattice strain. The Williamson–Hall plot of ZnO is shown in the inset of Fig. 2. The strain was calculated from the slope of the line, and the average crystallite size of the particles (D_{W-H}) can be evaluated from the interception with the y-axis of the line. The values of the mean crystallites size and the stress (micro-deformations) are 69.3 nm and 0.00155, respectively. The network parameters (a , c) and the unit cell volume (V) for the sample were determined using the following equations: [21]

$$a = \frac{\lambda}{\sqrt{3} \sin \theta_{(100)}}$$

$$c = \frac{\lambda}{\sin \theta_{(002)}}$$

$$V = \frac{\sqrt{3}}{2} a^2 \cdot c$$

The calculated lattice parameters values are $a = 3.2493 \text{ \AA}$, $c = 5.2049 \text{ \AA}$, and the volume of the unit cell is $V = 47.589 \text{ \AA}^3$. Figure 3 shows FE-SEM images and

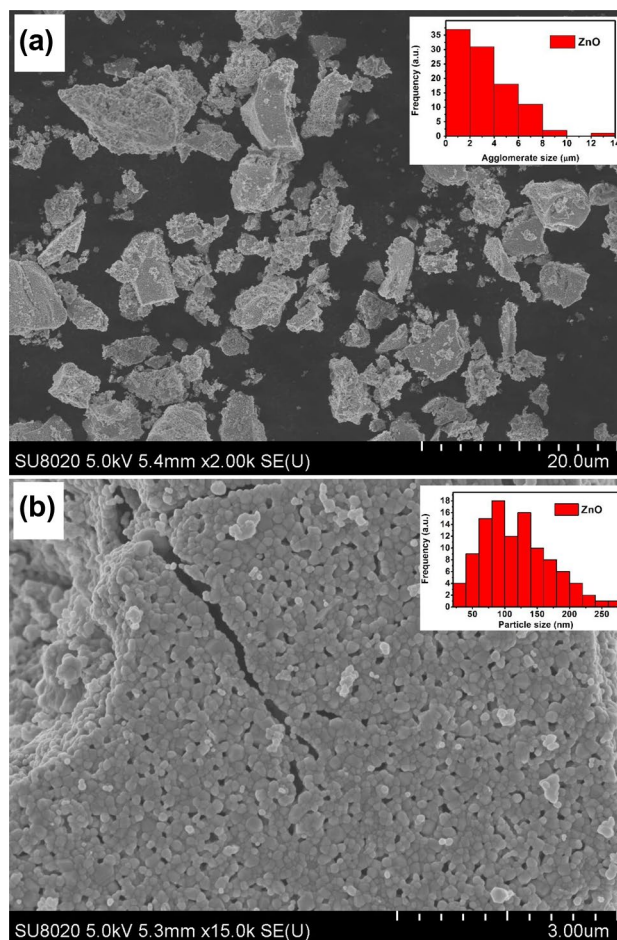


Fig. 3 SEM images of ZnO with (a) 20 μm and (b) 3 μm scales

the frequency (inset) as a function, estimated by image J, of the grain size for the ZnO sample. Figure 3a shows the agglomerates, with an average size of 3.28 μm . These agglomerates are composed by a uniform distribution of spherical grains with an average size equal to 76.86 nm (Fig. 3b). When assuming that all the particles are spherical, the specific surface (S) has been calculated from the relation: [20]

$$S = \frac{6000}{D \cdot \rho_{X\text{-ray}}} \quad \text{where} \quad \rho_{X\text{-ray}} = \frac{2 \cdot M}{N_A \cdot V} \quad (5)$$

where the constant “6000” is called the form factor for spherical particles, “ $\rho_{X\text{-ray}}$ ” is the X-ray density, and D is the diameter of the particle. “ N_A ” the Avogadro’s number, “ M ” is the molecular weight of the compound, “ V ” is the volume, and the number “2” represents the number of molecules in the unit cell of hexagonal wurtzite lattice. The high value, 24 m^2/g , of the specific surface area of ZnO nanoparticles is needed for sensing application [24, 25].

The Raman spectra of ZnO nanopowders is illustrated in Fig. 4. The number of active modes, as indicated in Table 1, indicates different modes of atomic displacement. The modes are divided into two models, depending on the polar branches, into a longitudinal optical (LO) and transverse optical (TO) components with different frequencies due to the macroscopic electric fields associated with phonons. However, the basic phonon modes of hexagonal ZnO were obtained at 102, 387, 439 and 583 cm⁻¹, which represents the E_{2L}, A₁-TO, E_{2H} and E₁-LO, respectively. The second-order phonon mode has occurred at about 150 cm⁻¹ which is attributed to 2E_{2L}. The multi-phonon diffusion modes are presented at 331, 508, 664 and 1065 cm⁻¹ which are assigned to 3E_{2H} - E_{2L}, E₁ (TO) + E_{2L}, 2 (E_{2H} - E_{2L}) and A₁ (TO) + E₁ (TO) + E_{2L}, respectively. Models A₁, E₁ and E₂ are active first-order Raman modes. The spectrum is somewhat complicated by the presence of some well-resolved multi-phonon features, in particular, one at around 200 cm⁻¹ (from low E₂ mode) and one at around 333 cm⁻¹ (due to the E₂^{high} combination E₂^{low}), of comparable intensity and similar in shape to the first-order peaks. The peak around 273 cm⁻¹ is attributed to the presence of a defect in our structure which is probably caused by the breakdown of translational crystal symmetry induced by a local electric field at the grain boundaries, with the consequent activation of otherwise silent modes.

FTIR spectra of ZnO powders, through KBr pellet method, presented in Fig. 5, exhibit several absorption bands. The 1533 cm⁻¹ and 1373 cm⁻¹ correspond to the symmetric and asymmetric C=O stretching vibration, respectively [26]. The bond at 998 cm⁻¹ is due to the C-O stretching vibration. The absorption at 879 cm⁻¹ is due to the formation of tetrahedral coordination of Zn. The observed peak in 684 cm⁻¹ indicates the stretching vibrations of ZnO nanoparticle [26]. The presence of carbon chemical

Table 1 Raman modes of wurtzite ZnO crystal

Wavenumber (cm ⁻¹)	Symmetry
~102	E ₂ ^{low}
~155/~204	2E _{2L}
~273	Defects
~333	3E _{2H} ⁻ E _{2L} Multi-phonon
~387	A ₁ -TO
~439	E ₂ ^{high}
~583	E ₁ -LO

The range of frequency variability is based on literature data [22, 23]

notations in our structure is linked to its strong presence in the precursor and the fuel used in the elaboration section.

The XPS spectra were investigated to have more information about the elemental constituents in the ZnO surface. The core levels of C 1 s, Zn LMM, O 1 s and Zn 2p are detected and showed in Fig. 5a–d, respectively. All XPS spectra have been deconvoluted using a Gaussian fit. The indexed peaks are tabulated in Table 2 with their area values and its corresponding components. In the C1s XPS spectra (Fig. 6a), it can be discerned three distinct peaks. The peaks at 283.13 eV and 284.65 eV are attributed to carbon atoms linked to the "C=C" network or the strong distortion of the crystal lattice caused by the fixation of oxygen-containing groups (C–C) [27]. The peak at 286.06 eV is related to hydroxyl and epoxide groups (C–OH and C–O–C) [28]. The total area of the spectrum C 1 s has a negligible value (835) compared to the other spectra Zn LMM (35,576), O 1 s (11,527) and Zn 2p3 (50,204) which indicates that there is a weak presence of the chemical elements linked to carbon and thereafter the high purity of our material. The observation of Auger lines Zn LMM, presented in Fig. 6b,

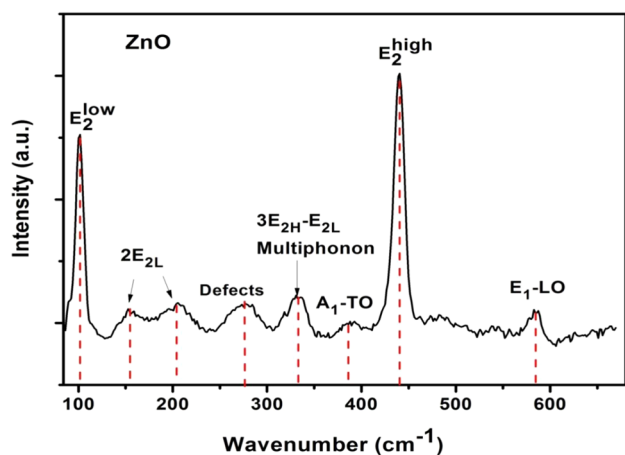


Fig. 4 Raman spectra of ZnO

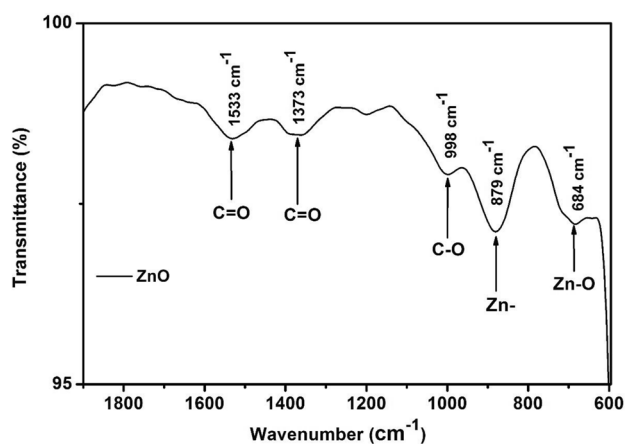


Fig. 5 FTIR spectrum of ZnO

Table 2 Peaks positions, area values and corresponding component of the deconvoluted XPS spectra of ZnO sample

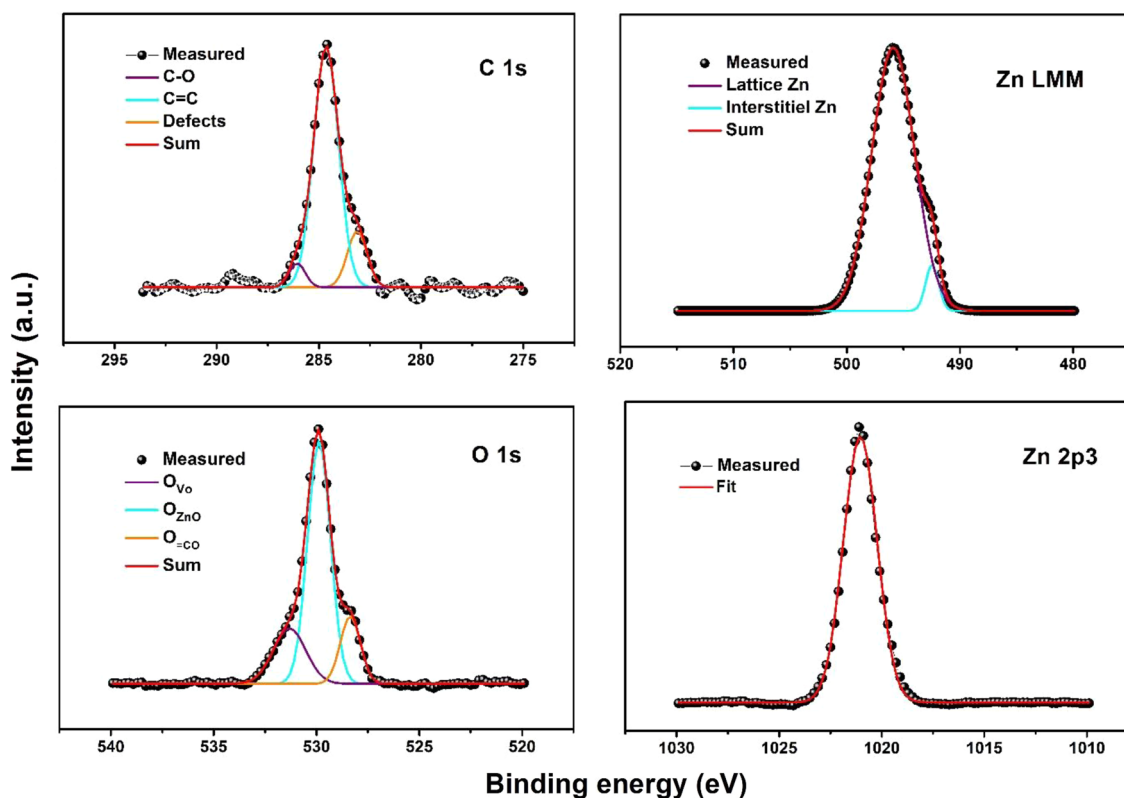
	Binding energy (e.V)	Area	Component
C 1 s	286.06	43	C–O
	284.65	668	C=C/C–C
	283.13	124	Defects
Zn LMM	495.90	33,778	Lattice Zn
	492.46	1798	Interstitial Zn
O 1 s	531.31	2385	Oxygen vacancies (V_o)
	529.88	7346	Zn–O
	528.35	1796	=CO
Zn 2p3	1021.05	50,204	Zn 2p 3/2

indicates the existence of interstitial Zn (Zn_i) defects. The two fitted Gaussian peaks are attributed to the presence of Zn in the O–Zn bond and to the interstitial Zn_i , these are located basically at the upper bond energy 495.90 eV and at the bond energy less 492.46 eV, respectively. The O1s signal showed in Fig. 6c has deconvoluted into three sub-components located at 528.33, 529.87 and 531.16 eV. The high band energy peak (531.16 eV) is associated with the oxygen vacancies, and the 529.87 eV peak is assigned to

the oxygen network in the hexagonal structure of ZnO [29, 30]. The last peak with lower binding energy (528.3 eV) is attributed to oxygen in =CO groups [31]. The spectrum Zn 2p3, in Fig. 6d, presents a peak located at 1021.1 eV which it corresponds to 2p 3/2. This can confirm the existence of Zn^{2+} ions in our composites. We can conclude from basic levels of Zn and O that there is a high presence of double donor defects (oxygen vacancies and Zn interstitials) in our sample, which improves gas detection performance [32, 33].

3.2 UV–Vis-NIR characterization

Gas detection properties are related to the range of UV–Visible light response and will be greatly improved as the range of light absorption is extended. It is important to see the absorbance rate in the different wavelengths since the large absorbance causes more generation of the electrons which subsequently participated in the gas detection mechanism. Thereafter, it is necessary to carry out a UV–Vis characterization to evaluate the optical properties [34]. The NO_2 gas detection tests were carried out under light illumination (UV, Purple, Blue and green lights); The UV–Vis-NIR absorption and reflectance spectra in the 200–1800 nm range of ZnO have investigated, and the results were presented in Fig. 7a. The absorbance is higher in the UV range (200–400 nm)

**Fig. 6** XPS spectra C 1 s, Zn LMM, O 1 s and Zn 2p3 of the ZnO sample

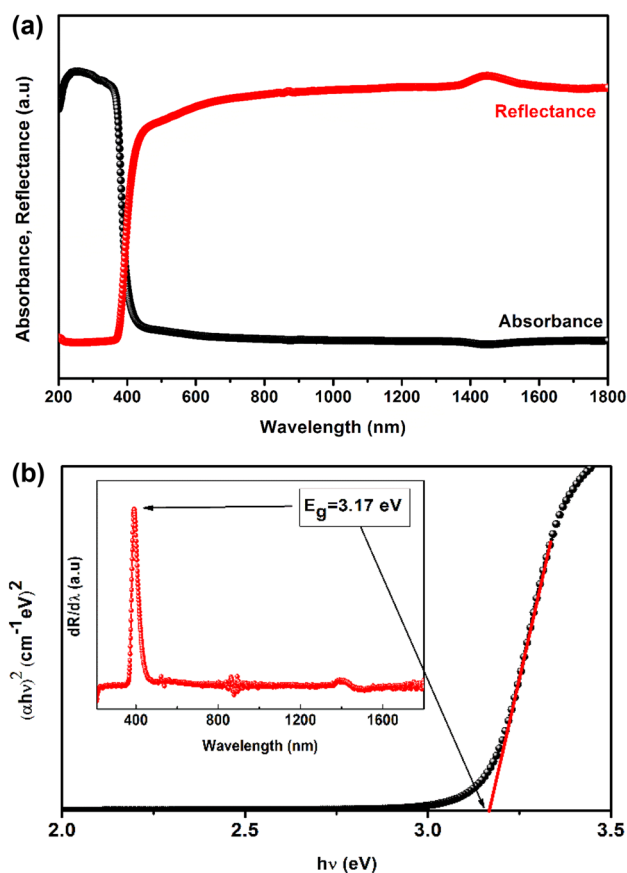


Fig. 7 (a) Absorbance, reflectance spectra of ZnO. (b) Tauc plot and $dR/d\lambda$ vs. wavelength of ZnO sample prepared by auto-combustion method

and for wavelengths greater than 400 nm, it is observed a remarkable decrease in absorbance in the visible and near-infrared ranges. This result is confirmed by the reflectance spectrum which has a value of less than 5% in the UV range such that the absorbance in this region is the highest. On the other hand, the reflectance has more than 80% in the visible-NIR range, which confirms that the light diffusion power is important in this range. We have investigated the variation of $(\alpha h\nu)^2$ as a function of the energy of the photons, presented in Fig. 7b, which was according to Tauc's model [35]:

$$\alpha h\nu = A(h\nu - E_g)^n \quad (6)$$

in which α , h and ν are absorption coefficient, Planck constant and photon frequency, respectively. A is a constant and $n = 1/2$ for the material with a direct bandgap. The estimated value of gap energy from Tauc's model was 3.17 eV. Also, the bandgap value can be estimated using the first derivative of the reflectance ($dR/d\lambda$), illustrated in Fig. 7b. The bandgap value corresponds to the wavelength $\lambda = 391$ nm. Thus, it can be concluded that photonic energy with a wavelength

less than 391 nm allows the emission of electrons from the valence band to the conduction band. The estimated gap energy value from this method is very close to that defined by Tauc's model. This will allow the generation of electrons which will be part of the target gas detection mechanism. To have the effect of the wavelength in the detection mechanism, we chose the lights which have a wavelength close to 391 nm. We carried out the gas tests under UV ($\lambda \approx 380$ nm), purple ($\lambda \approx 400$ nm), blue ($\lambda \approx 480$ nm) and green ($\lambda \approx 530$ nm) lights.

3.3 Electrical investigation

The ac conductivity, σ_{ac} , of the ZnO spectrum considered is given in Fig. 8. The conductivity depends on the frequency and temperature, increasing with the rise of both parameters. This behavior, associated with the conductivity values registered, indicates that our sample is a semiconductor, as expected. With the increase of the temperature, the ac conductivity becomes frequency independent exhibiting a plateau. This plateau which extends to lower frequencies with the temperature increase is the *dc*-conductivity, σ_{dc} , originated by the charge carriers translational motion, described by the empirical Jonscher law [36]:

$$\sigma_{ac} = \sigma_{dc} + A\omega^S \quad (7)$$

Where A is a constant, ω is the angular frequency, and S is the power-law exponent being between 0 and 1. The temperature dependence of the exponent S is shown in Fig. 9a. As we can notice that this parameter was decreasing with an increase of temperature and attains a minimum value than further increases which can be suggested that the conduction be mediated by overlapping large polaron tunneling (OLPT) process [37]. The thermal variation of σ_{ac} at 100 Hz is shown in Fig. 9b. It adapts well to the small polaron hopping pattern (SPH), which is expressed by the equation [38]:

$$\sigma \cdot T = A \cdot \exp\left(-\frac{E_a}{k_B T}\right) \quad (8)$$

Where E_a is the activation energy of the moving charge carriers and k_B the Boltzmann constant. The estimated activation energy value in the range 200–400 K, indicates two different values. This value increases in the high-temperature range. It is assumed that at low temperature the electrical activation energy refers to the Zn jump between interstitial sites, while processes with higher activation energy are due to the site oxygen vacancy jump normal to an equivalent vacancy [39]

The real part of the impedance, Z' , versus the frequency at several temperatures is shown in Fig. 10a. The low-frequency plateau shifts as the temperature increases, while the high-frequency plateau is almost independent of

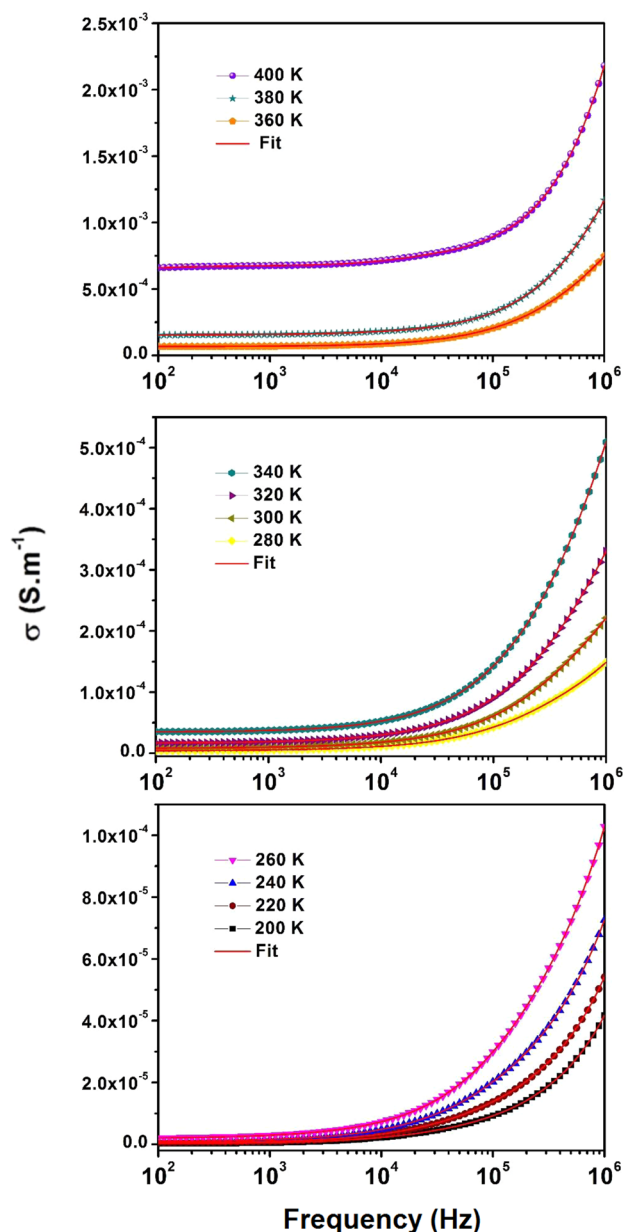


Fig. 8 Conductivity spectrum over wide temperature range

temperature. The high value of Z' at low-frequency means that most of the charge carriers did not receive enough energy to jump the grain boundaries. The continuous temperature rise energizes some of them, which become able to cross the grain boundaries. This explains why Z' gradually decreases with temperature. Thus, the low value of Z' at high-frequency indicates that the mobile carriers no longer experience grain boundary restriction. In conclusion, charged particles accumulate around integrations at low frequencies, forming a space charge which degenerates with frequency [40]. The slow decrease of Z' over the dispersive region is a signature of the polarization of the space

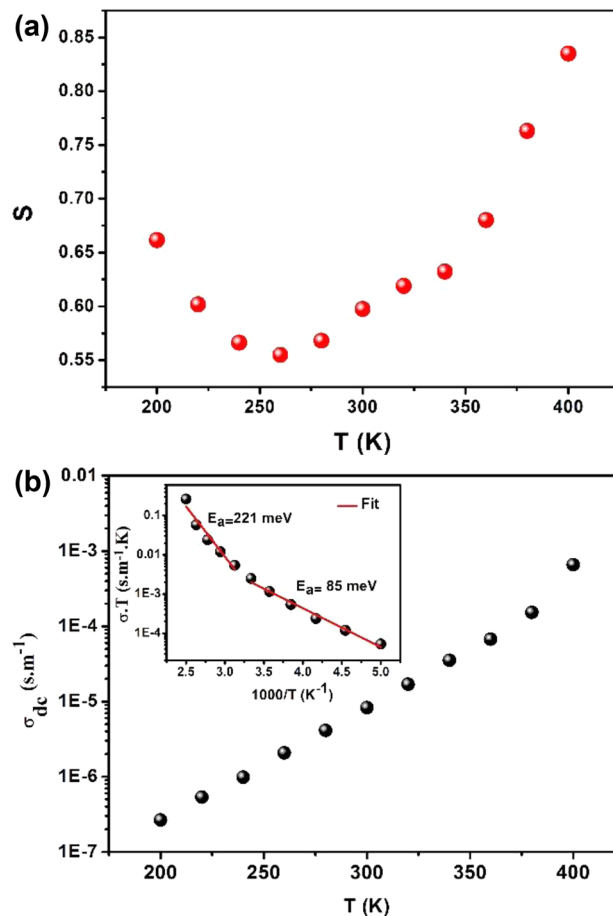


Fig. 9 Temperature dependence of the (a) power-law exponent, S , and (b) dc-conductivity, with the activation energy, by plotting σT vs. $1000/T$ (inset plot)

charge according to Ranjan et al. [41]. The dependence of the imaginary part of the impedance, Z'' , with the frequency in the wide temperature range is shown in Fig. 10b, in which one peak is visible, corresponding to a dielectric relaxation phenomenon. The frequency corresponding to the Z'' maximum, relaxation frequency, shifts to higher frequencies with the temperature rise. Moreover, with the increasing of the temperature the Z'' maximum decreases, being this tendency typical of ZnO [42].

The Nyquist diagram of the zinc oxide is shown in Fig. 11a. The graph, at each temperature, is a semicircle, whose diameter continuously decreases with the increasing of temperature. In this representation, pure resistivity, R , can be extrapolated through the Z' value, at lowest frequency. [43]. The complex impedance Z^* can be expressed by:

$$Z^*(\omega) = Z'(\omega) - jZ''(\omega) \quad (9)$$

which Z' and Z'' are, respectively, the real and imaginary parts. The resulting semicircle were centered below the

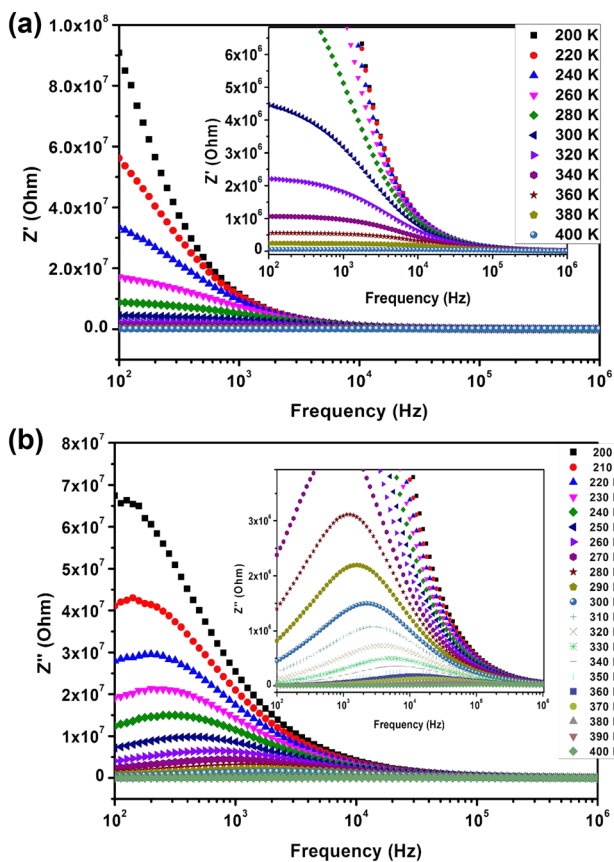


Fig. 10 Frequency dependence of the complex of impedance (Z^*): (a) the real part of impedance (Z') and (b) the imaginary part (Z'')

Z' axis, suggesting non-Debye dielectric relaxation. This behavior of the Nyquist diagram can be attributed to the heterogeneity of the material [44]. According to the Koops model [45], the conductivity of a semiconductor is governed by high conductive grains, at high frequencies (left side), and grain boundaries, at low frequencies (right side). The electrical response of our ZnO powders can be modeled by an equivalent circuit formed by a two series combination of grains boundary (R_{gb} - CPE_{gb}) and grains (R_g). The impedance data, at room temperature, are fitted using Z-view software [46]. Figure 11b indicates that the experimental data is well fitted which confirms the validity of the equivalent circuit obtained. The constant phase element (CPE) is represented by the following equation [47]:

$$Z_{CPE} = \frac{1}{Q(i\omega)^\alpha} \tag{10}$$

where Q , ω and α are, respectively, the proportional factor, the angular frequency and the parameter. α is an estimate of the deviation from the ideal capacitive behavior. when it is zero, we see a pure resistive behavior and when it is of value 1, we see a capacitive behavior. The obtained values

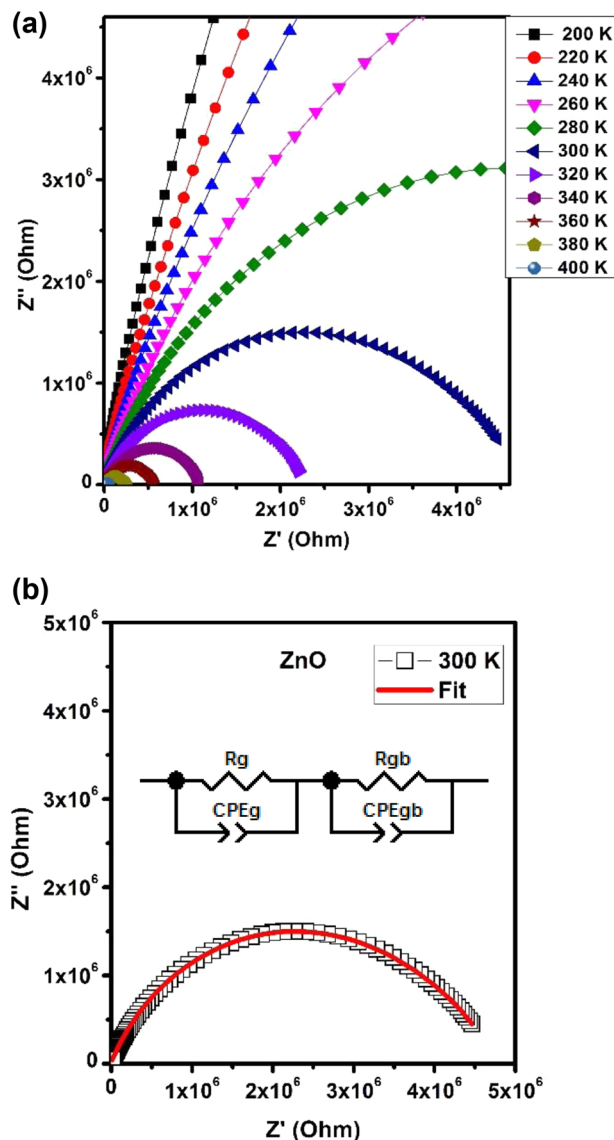


Fig. 11 (a) Nyquist diagram at different temperatures. (b) Experimental and theoretical impedance diagrams of ZnO nanoparticles at room temperature with equivalent circuit model (inset)

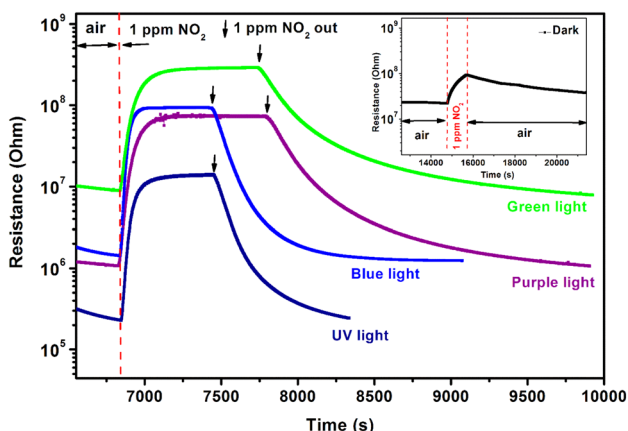
from the grain's resistance R_g , capacitance CPE_g , and α_g , and from the grains boundary's resistance R_{gb} , capacitance CPE_{gb} , and α_{gb} , determined at room temperature are presented in Table 3.

3.4 NO₂ sensing tests

The sensing test was investigated under light illumination, source of energy activation, at room temperature to activate the surface reactions. The electrical resistance of the sensors based on ZnO composite, illuminated by lights of various wavelengths ranging from 380 to 530 nm, was presented as a function of time during injections of 1 ppm of NO₂ (Fig. 12).

Table 3 Fitting parameters of the Nyquist diagram for ZnO at room temperature

R_g (Ohm)	10^3
CPE_g (F)	10^{-6}
α_g	0.99
R_{gb} (Ohm)	$4.7 \cdot 10^6$
CPE_{gb} (F)	10^{-11}
α_{gb}	0.72

**Fig. 12** (a) Room temperature sensor resistance versus time to 1 ppm NO₂ of ZnO under green, blue, purple and UV light illumination. (b) Mechanism of dioxygen reaction with ZnO surface under the illumination of different lights

The illumination plays an important role in the performance of the sensor. The inset in Fig. 9a shows the slow and weak response of the sensor when in the dark. Some characteristics are determined from this curve and tabulated in Table 4. The resistance R_{air} decreased when the light wavelength went from 530 to 380 nm. It was diminished from $2.22 \cdot 10^7 \Omega$ in the dark to $2.31 \cdot 10^5 \Omega$ when illuminated by UV light. The increase in photonic energy agrees with the decrease in the light wavelength according to the equation $E = hc/\lambda$ [4, 7]. As a result, when the light wavelength is shortened causes more electron–hole pairs to be generated on the ZnO surface and photodesorption of the adsorbed oxygen, which results in a reduction of the electrical resistance.

Table 4 Room temperature sensor response and response/recovery times of ZnO in 1 ppm of NO₂ under different lights illumination and 50% of humidity

Wavelength	Light color	R_{air} (Ohm)	Response ($(R_{NO_2} - R_{air})/R_{air}$)	Response time (min)	Recovery time (min)
–	Dark	$2.22 \cdot 10^7$	3.2	10.1	Over 60
530 nm	Green	$9.03 \cdot 10^6$	54	5	8.3
480 nm	Blue	$1.43 \cdot 10^6$	53	1.5	1.9
400 nm	Purple	$1.07 \cdot 10^6$	90.7	4	6.7
380 nm	UV	$2.31 \cdot 10^5$	88.2	4.4	3.3

Figure 13a–d presents the sensor response as a function of the time under different NO₂ concentrations (0.5, 0.75 and 1 ppm) at room temperature illuminated by green, blue, purple and UV lights, respectively. The sensor presents, under different wavelengths, linear responses as a function of the NO₂ concentration, as shown in the insets of Fig. 13.

The ZnO sensor has high responses at 1 ppm NO₂ when UV and purple light has been used to be the maximum response when illuminated by purple light. However, the response and recovery times were relatively longer compared to those with blue light. Subsequently, a compromise between sensitivity and response/recovery times of the sensor must be made. To get a short response and recovery times, we could say that the blue light can be the best choice for the ZnO-based sensor.

3.5 Sensing mechanism

When the ZnO sensor was exposed to humid air under dark conditions, the active surface of ZnO material was covered with chemisorbed and physisorbed species. ZnO is a known n-type semiconductor due to its oxygen vacancies [6, 17]. Those free electrons can be trapped by oxidizing gases. In the presence of air and water vapor, the main species adsorbed on the surface are oxygen. Among the oxygen species (O_2^- , O^- , O^{2-} and OH^-) adsorbed on the surface, the O_2^- is dominant at room temperature [48]. Again, the oxygen adsorbed on the surface can trap the electrons from the conduction band (CB). Therefore, free electrons in the conduction band will be captured by oxygen molecules adsorbed on the zinc oxide surface to form oxygen species (O_2^-).



We have the formation of a depletion layer on the surface of ZnO grains, which increases the resistance of the film. Since the sensitive layer is made of small grains, the electrons must jump across a potential barrier between the grains. As the overall resistivity of the layer is conditioned by the

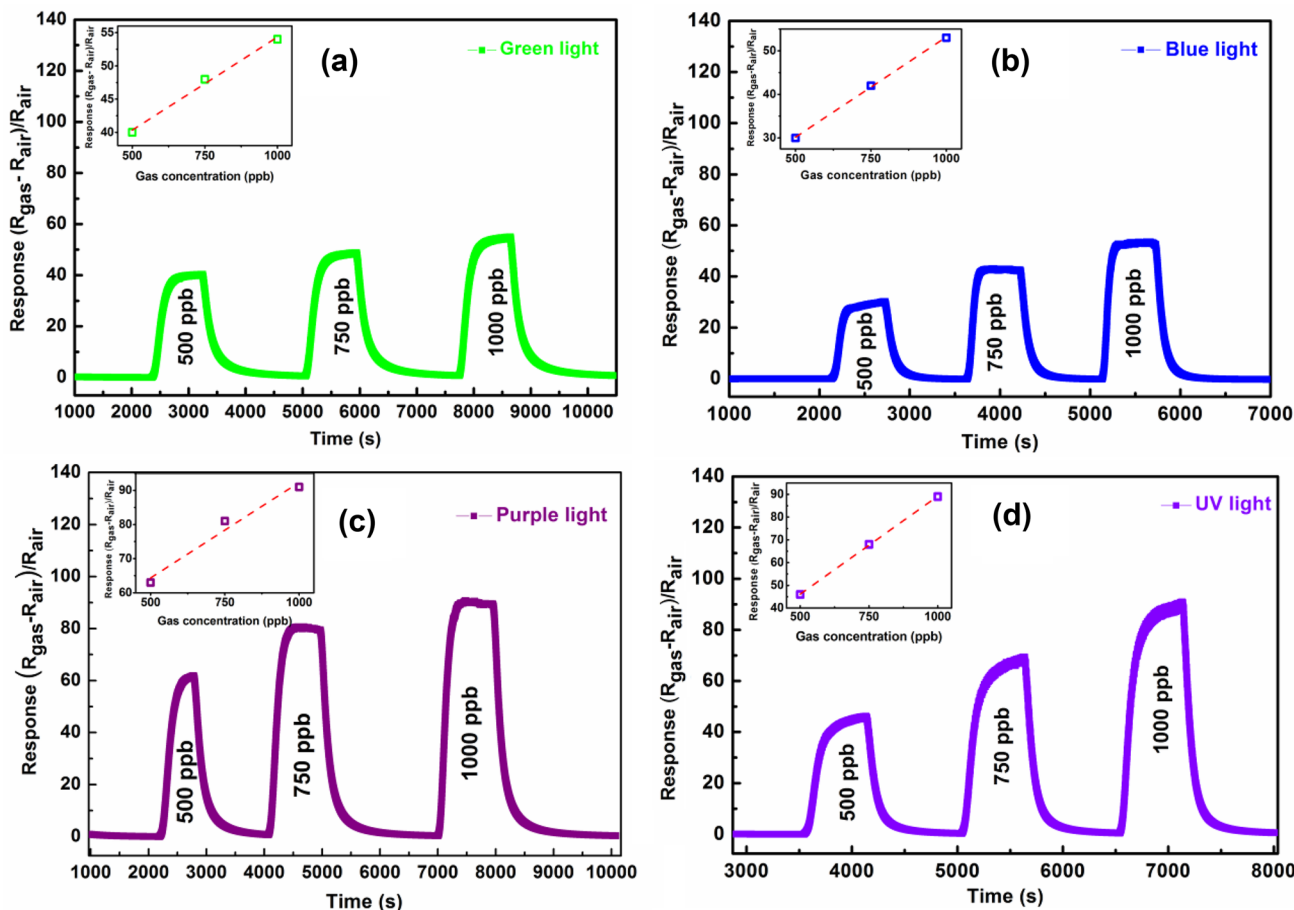


Fig. 13 Sensor response versus time of ZnO under (a) green (b) blue, (c) purple and (d) UV light illumination at room temperature

contact resistance between the grains. The conductance can be expressed by:

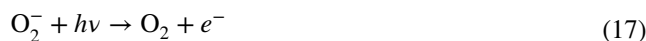
$$G = G_0 \exp\left(-\frac{e \cdot V_s}{k_B \cdot T}\right) \quad (13)$$

Equation (13) presents the role of the potential barrier which is linked to the quantity of molecule adsorbed per unit area. When the partial pressure of oxygen or the temperature decreases O₂⁻ can decompose into O₂ and e⁻ released to the semiconductor. The effects of light on the detection properties of the metal oxide sensor have been studied by several researchers [49, 50]. To explain the results, consider the photodesorption of the oxygen adsorbed such that photo-generated electron-hole pair can release the O₂⁻ ion and create photo-generated oxygen ions, according to the following equations O₂⁻ (hv) [50].



According to this model, it is observed emission of electrons from the valence to the conduction band. The energy required for band-to-band excitation depends on the bandgap energy of ZnO which is calculated from the Tauc model and equal to 3.17 eV. Photonic energy was determined by the light wavelength ($E = hc/\lambda$). This means that the photonic energies of wavelength 380 nm (3.3 eV) and 400 nm (3.1 eV) were enough to band-to-band excitation of ZnO. The model looks perfect for the lighting of $\lambda \leq 400$ nm but does not explain the behavior for longer wavelengths.

It was reported [51, 52] that the striking photon is directly absorbed by the oxygen species O₂⁻ from the surface, which causes the desorption of O₂⁻ and a release of the electron trapped in the material.



This reaction (photodesorption) requires less energy and may be possible for longer wavelengths. The energy required for the adsorption of an oxygen atom on a metal oxide is

approximately 1.5 eV [53]. Such a reaction is possible because the photons of the light sources used are sufficiently energetic, even for green light 530 nm (2.3 eV). Subsequently, we can say that the reactions (15) and (16) are reversible, which means that the adsorption of O₂ under bright lighting could reach a new equilibrium.

Langmuir's adsorption model is the first approach to model the response and recovery times. If A is the surface concentration in adsorption sites, the surface coverage can be defined as the fraction of sites occupied by the adsorbate.

$$\theta = \frac{[X^*]}{A} \quad (18)$$

$$\frac{d\theta}{dt} = r_{\text{ads}} - r_{\text{des}} \quad (19)$$

$$r_{\text{ads}} = K_{\text{ads}} \cdot (1 - \theta) \cdot p \quad (20)$$

$$r_{\text{des}} = K_{\text{des}} \cdot \theta \quad (21)$$

Which

$$K_{\text{ads}} = K_{\text{ads}}^0 \exp\left(\frac{-E_{\text{ads}}}{k_{\text{B}}T}\right) \quad (22)$$

$$K_{\text{des}} = K_{\text{des}}^0 \exp\left(\frac{-E_{\text{des}}}{k_{\text{B}}T}\right) \quad (23)$$

where K_{ads} and K_{des} are the adsorption and the desorption coefficients, respectively. P_A is the partial gas pressure which, in this case, is a constant. k_{B} and T are Boltzmann constant and the temperature; E_{ads} and E_{des} are the adsorption and desorption activation energies, respectively; K_{ads}^0 and K_{des}^0 are desorption and adsorption constants, respectively. At equilibrium, we can express the surface fraction occupied by the gas θ by the following equation

$$\theta = \frac{KP_A}{KP_A + 1} \quad (24)$$

In which K is the adsorption constant and expressed by:

$$K = \frac{K_{\text{ads}}}{K_{\text{des}}} = \frac{K_{\text{ads}}^0}{K_{\text{des}}^0} \exp\left(\frac{Q_{\text{ads}}}{k_{\text{B}}T}\right), \quad \text{which} \quad Q_{\text{ads}} = E_{\text{des}} - E_{\text{ads}} \quad (25)$$

Adsorption and desorption times (related to, respectively, the response and recovery times) are expressed by:

$$\tau_{\text{ads}} = \frac{1}{K_{\text{ads}}P_A + K_{\text{des}}} \quad (26)$$

$$\tau_{\text{des}} = \frac{1}{K_{\text{des}}} \quad (27)$$

According to this model, the sensitivity and response/recovery times strongly depend on the temperature. ZnO has a strong affinity for oxygen or NO₂ and therefore, the adsorption energy and desorption energy is big. Therefore, at room temperature, the kinetic constants in Eqs. 24 and 25 are smaller, resulting in long response and recovery times. The sensitive material must be heated (typically around 250 °C) to increase the kinetics.

The adsorption or desorption can be accelerated using an external energy source such as light.

The above coefficients (θ , K , τ_{ads} and τ_{des}) can be modified with the addition of a term because of the light which the two coefficients K_{ads} and K_{des} will be expressed by [32].

$$K_{\text{ads}} = K_{\text{ads}}^0 \exp\left(\frac{-E_{\text{ads}}}{k_{\text{B}}T}\right) + K_{\text{ads}}^1(\lambda, I) \quad (28)$$

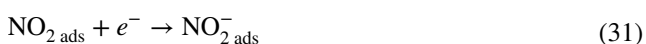
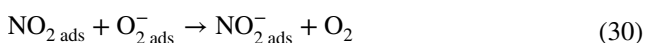
$$K_{\text{des}} = K_{\text{des}}^0 \exp\left(\frac{-E_{\text{des}}}{k_{\text{B}}T}\right) + K_{\text{des}}^1(\lambda, I) \quad (29)$$

which K_{ads}^1 and K_{des}^1 are the factors related to photonic energy, associated with the photon energy and intensity of light. These additional terms make it possible to obtain faster kinetics thanks to the light effect. The role of photonic energy on the time of detection mechanism is like heating, which improves the K_{ads} and K_{des} of O₂⁻ and improves the response and recovery times. The lights make it possible to increase the kinetics of adsorption and desorption and consequently to reduce the response/recovery times.

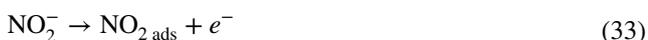
The light effect on the detection mechanism can be ascribed to the change in electrical resistance. When the sensor is exposed to humid air under dark, oxygen species adsorbed on the surface will capture the free electrons of the conduction band which will create a depletion layer. Secondly, the sensor is exposed to air containing a ppm-level of NO₂ concentrations. The NO₂ molecules will be absorbed by the surface and capture the electrons from the surface of ZnO to form NO₂⁻ species, which causes an increase in the height of the potential barrier and subsequently leads to an increase in the electrical resistance value of the material. Also, NO₂ competition takes place on the surface of the semiconductor with the oxygen already adsorbed, which means that more electrons will be captured in the conduction band (CB) to form NO₂⁻ species and then we obtain an increase in the resistance of the sensor. The interaction of NO₂ with the oxygen species adsorbed on the surface of ZnO is a powerful chemisorption process that can capture more electrons from the conduction band. It has been suggested that upon exposure to NO₂, the bound electrons of O₂⁻ adsorbed on the surface of ZnO is transferred to physisorbed NO₂.

Table 5 Performance of ZnO as room temperature (RT) NO₂ sensor in comparison with ZnO literature results

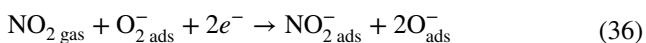
Materials	Fabrication method	Light illumination	NO ₂ (ppm)	Response	Response/recovery times (min)	Reference
ZnO	Thin film	Dark	20	119	1.42/1.76	[58]
ZnO	Drop-cast	UV	5	1.1	1.5/5	[59]
ZnO	H ₂ O ₂ treatment & annealing	White	0.9	5.3	1.8/2.7	[60]
ZnO	Facile solution & annealing	UV	5	2.5	0.5/1.5	[61]
rGO-ZnO	Hydrothermal	White	0.1	4.66	1.5/2.5	[32]
ZnO	Soft e-beamlithography	UV	20	2.2	15/5	[62]
ZnO	Sputtering	UV	0.5	8	–/–	[63]
ZnO	Auto-combustion	Purple	1	90.7	4/6.7	This work



When physisorbed NO₂ accepts the electron from O₂[−], a stable state of chemisorbed NO₂[−] is created. It is well known that NO₂[−] forms deeper surface acceptor levels than the oxygen ion O₂[−] and increases the thickness of the depletion layer [54]. Under conditions of darkness at room temperature, O₂[−] is stable, and the NO₂ molecules do not easily extract the electrons from O₂[−] to form NO₂[−]. Thereafter, the reaction (30) is slow, and the response time becomes long. When NO₂ is removed, the electron is transferred from



Equation (32) is the inverse of Eq. (30). This reaction is not easy to carry out, because the desorption of NO₂[−] is very slow at room temperature. So, the recovery time is also very long in the dark which is confirmed in Table 4. In another way, the molecules of NO₂ can react with the oxygen ions adsorbed on the surface according to the following reactions, and thereby the resistance of the detection material increase [55, 56]:



Under lighting, the light-illuminated ZnO sensors show a short response and recovery times which should reflect the reaction speed between O₂[−] and NO₂. When NO₂ becomes on the surface of ZnO under light illumination, the adsorption rate of NO₂ on the surface of ZnO is improved by light. If we consider that the reaction between O₂[−] and NO₂ as a

process of adsorption of NO₂ on the O₂[−] site, the response time can be considered as the adsorption time of O₂[−].

We can see in Table 4 that the response of the sensor is increased when the light wavelength is shortened.

Lights at 380 and 400 nm can cause additional reactions with NO₂. The conversion of the NO₂ molecule to O₃ and NO under a light wavelength less than around 480 nm has been confirmed by the measurement of photolysis-chemiluminescence [57] via:



The O atom formed by Eq. (37), with the presence of air, reacted with O₂ to form ozone molecular (O₃) which can react with NO to re-create NO₂.

This may explain why the sensitivity goes through a maximum for purple light and why the response time increases again for shorter wavelengths.

It was investigated the comparison between our sample and other ZnO-based NO₂ sensors studied in the literature. Table 5 presents our NO₂ gas sensor-based ZnO, at room temperature, compared to the other ZnO sensor prepared by other methods. This sensor shows a high response to NO₂ gas at sub-ppm level. Furthermore, it has an acceptable response/recovery times compared to other sensors.

4 Conclusion

In this study, it was prepared ZnO using the auto-combustion method. The measurement by X-ray diffraction indicated that our structure is hexagonal wurtzite with space group P6₃mc. The average size of the crystallites was calculated by Williams–Hall method which it exhibits the value of 69.3 nm. The surface morphology, by scanning electron

microscope, showed the presence of hexagonal agglomerates made up of nanometric particles which have an average size of 76.86 nm. The absorption and reflectance spectra in the UV–Vis–NIR range indicate a higher absorption in the UV range of ZnO powder, and the bandgap energy was calculated by Tauc model which was equal to 3.170 eV. FTIR investigation indicates the presence of chemical notations in our structure which is confirmed by the XPS (C 1 s) spectrum. The electrical conductivity can be described by Jonscher's law. We have investigated the gas sensing performances at room temperature under illumination with different light wavelengths to 0.5, 0.75 and 1 ppm NO₂ concentrations. It indicated that the sensor exhibits a high response and acceptable response/recovery times compared to the results obtained in the literature of ZnO elaborated by other methods. The best response was observed of the ZnO sensor under light with low wavelength 400 nm (purple) and 380 nm (UV). The obtained results seem promising for the development of a low-cost ambient temperature NO₂ gas sensors with this material.

References

- C. Zhang, M. Debliqy, A. Boudiba, H. Liao, C. Coddet, *Sens. Actuators B Chem.* **144**, 280–288 (2010)
- P. Su, T. Pan, *Mater. Chem. Phys.* **125**, 351–357 (2011)
- S. Wei, Y. Xing, Y. Li, Y. Zhao, W. Du, M. Zhou, *Vacuum* **129**, 13–19 (2016)
- C. Zhang, O. Overschelde, A. Boudiba, R. Snyders, M. Olivier, M. Debliqy, *Mater. Chem. Phys.* **133**, 588–591 (2012)
- H. Moon, S. Han, M. Kang, W. Jung, B. Kwon, C. Kim, T. Lee, S. Lee, S. Baek, J. Kim, H. Park, C. Kang, *Sens. Actuators B* **229**, 92–99 (2016)
- M. Benamara, J. Massoudi, H. Dahman, E. Dhahri, L. El Mir, A. Ly, M. Debliqy, D. Lahem, *J. Mater. Sci.: Mater. Electron.* **31**(17), 14249–14260 (2020)
- X. Geng, C. Zhang, M. Debliqy, *Ceram. Int.* **42**, 4845–4852 (2016)
- J. Zhang, X. Liu, G. Neri, N. Pinna, *Adv. Mater.* **28**, 795–831 (2016)
- W.Z. Wang, T. Coyle, D. Zhao, *J. Therm. Spray. Technol.* **23**, 827–832 (2014)
- J. Saura, *Sens. Actuators B: Chem.* **17**, 211–214 (2001)
- P. Camagni, G. Faglia, P. Galinetto, C. Perego, G. Samoggia, G. Sberveglieri, *Sens. Actuators B Chem.* **31**, 99–103 (1996)
- E. Comini, G. Faglia, G. Sberveglieri, *Sens. Actuators B Chem.* **78**, 73–77 (2001)
- B.P.J. de Lacy Costello, R.J. Ewen, N.M. Ratcliffe, M. Richards, *Sens. Actuators B Chem.* **134**, 945–952 (2008)
- K. Anothainart, M. Burgmair, A. Karthigeyan, M. Zimmer, I. Eisele, *Sens. Actuators B: Chem.* **93**, 580–584 (2003)
- J.D. Prades, R. Jimenez-Diaz, F. Hernandez-Ramirez, S. Barth, A. Cirera, A. Romano-Rodriguez et al., *Sens. Actuators B Chem.* **140**, 337–341 (2009)
- C. Zhang, A. Boudiba, P. De Marco, R. Snyders, M.G. Olivier, M. Debliqy, *Sens. Actuators B: Chem.* **181**, 395–401 (2013)
- M. Benamara, E. Gómez, R. Dhahri, A. Serrà, *Toxins* **13**, 66–82 (2021)
- X. Geng, J. You, C. Zhang, *J. Alloys Compd.* **687**, 286–293 (2016)
- J. Rodríguez-Carvajal, *Physica B* **192**(1–2), 55–69 (1993)
- D. Bouokkeze, J. Massoudi, W. Hzez, M. Smari, A. Bougoffa, K. Khirouni, L. Bessais, *RSC Adv.* **9**(70), 40940–40955 (2019)
- D.K. Dubey, D.N. Singh, S. Kumar, C. Nayak, P. Kumbhakar, S.N. Jha, D. Bhattacharya, A.K. Ghosh, S. Chatterjee, *RSC Adv.* **6**(27), 22852–22867 (2016)
- V. Russo, M. Ghidelli, P. Gondoni, C.S. Casari, A. Li Bassi, *J. Appl. Phys.* **115**(7), 073508 (2014)
- D.N. Montenegro, V. Hortelano, O. Martínez, M.C. Martínez-Tomas, V. Sallet, V. Muñoz-Sanjosé, J. Jiménez, *J. Phys. D: Appl. Phys.* **46**(23), 235302 (2013)
- E.R. Kumara, C. Srinivasb, M.S. Seehrac, M. Deeptyb, I. Pradeepe, A.S. Kamzin, M.V.K. Meharg, N.K. Mohanh, *Sens. Actuators A: Physic.* **279**, 10–16 (2018)
- S. Jaballah, M. Benamara, H. Dahman, A. Ly, D. Lahem, M. Debliqy, L. EL Mir, *Mater. Chem. Phys.* **31**(11), 8230–8239 (2020)
- K. Jhansi, N. Jayarambabu, K. P. Reddy, N. M. Reddy, R. P. Suvarna, K. V. Rao, B. Siva kumari, *Int. J. Multi. Adv. Res. Trends* **2**, 273–282 (2015)
- W. Li, G. Wang, C. Chen, J. Liao, Z. Li, *Nanomaterials* **7**(1), 20 (2017)
- J. Das, S.K. Pradhan, D.R. Sahu, D.K. Mishra, S.N. Sarangi, B.B. Nayak, S. Verma, B.K. Roul, *Phys. B* **405**(10), 2492–2497 (2010)
- X. Geng, C. Zhang, Y. Luo, M. Debliqy, *Appl. Surf. Sci.* **401**, 248–255 (2017)
- C. Zhang, X. Geng, H. Liao, C. Li, M. Debliqy, *Sens. Actuators B: Chem.* **242**, 102–111 (2017)
- A. Celebioglu, S. Vempati, C. Ozgit-Akgun, N. Biyikli, T. Uyar, *RSC Adv.* **4**(106), 61698–61705 (2014)
- X. Geng, P. Lu, C. Zhang, D. Lahem, M.G. Olivier, M. Debliqy, *Sens. Actuators B: Chem.* **282**, 690–702 (2019)
- S. Jaballah, M. Benamara, H. Dahman, D. Lahem, M. Debliqy, L. El Mir, *J. Mater. Sci.: Mater. Electron.* **31**(11), 8230–8239 (2020)
- B. Xu, Q. Zhang, S. Yuan, M. Zhang, T. Ohno, *Chem. Eng. J.* **260**, 126–132 (2015)
- B. Tiss, M. Erouel, N. Bouguila, M. Kraini, K. Khirouni, *J. Alloys Compd.* **771**, 60–66 (2019)
- K. Omri, I. Najeh, L. El Mir, *Ceram. Int.* **42**, 8940–8948 (2016)
- A. Ghosh, *Phys. Rev. B* **42**, 1388 (1990)
- A. Tabib, N. Sdiri, H. Elhouichet, M. Férid, *J. Alloys Compd.* **622**, 687–694 (2015)
- L. Chouiref, S. Jaballah, M. Erouel, N. Moutia, W. Hzez, I. Ghiloufi, L. El Mir, *J. Mater. Sci. Mater. Electron.* **31**(16), 13899–13908 (2020)
- N. Assoudi, W. Hzez, R. Dhahri, I. Walha, H. Rahmouni, K. Khirouni, E. Dhahri, *J. Mater. Sci. Mater. Electron.* **29**, 20113–20121 (2018)
- R. Ranjan, R. Kumar, N. Kumar, B. Behera, R.N.P. Choudhary, *J. Alloys Compd.* **509**, 6388–6394 (2011)
- A. Dhara, S. Sain, S. Das, S.K. Pradhan, *Ceram. Int.* **44**, 7110–7121 (2018)
- D. Sinclair, *Boletín la Soc. Española Cerámica y Vidr.* **34**, 55–65 (1995)
- R. Chtourou, B. Louati, K. Guidara, *J. Alloys. Compd.* **732**, 286–292 (2018)
- C.G. Koops, *Phys. Rev.* **83**, 121–124 (1951)
- D. Johnson, *ZPlot, Z-View Electrochemical Impedance Software, Version 2.3 b* (Scribner Associates Inc, North Carolina, 2000)
- F.B. Abdallah, A. Benali, S. Azizi, M. Triki, E. Dhahri, M.P.F. Graça, M.A. Valente, *J. Mater. Sci. Mater. Electron.* **30**(9), 8457–8470 (2019)
- N. Barsan, U.D.O. Weimar, *J. Electroceram.* **7**, 143–167 (2002)
- L. Deng, X. Ding, D. Zeng, S. Tian, H. Li, C. Xie, *Sens. Actuators B Chem.* **16**(3), 260–266 (2012)

50. A. Giberti, V. Guidi, C. Malagù, in: *The 14th International Meeting on Chemical Sensors*, 395–401 (2012)
51. A. Giberti, C. Malagù, V. Guidi, *Sens. Actuators B: Chem.* **165**, 59–61 (2012)
52. D. Haridas, A. Chowdhuri, K. Sreenivas, V. Gupta, *Sens. Actuators B: Chem.* **153**, 152–157 (2011)
53. M. Batzill, U. Diebold, *Prog. Surf. Sci.* **79**, 47–154 (2005)
54. H.-J. Lim, D.Y. Lee, Y.-J. Oh, *Sens. Actuators B: Chem.* **125**, 405–410 (2006)
55. S. Bai, D. Li, D. Han, R. Luo, A. Chen, C.L. Chung, *Sens. Actuators B: Chem.* **150**, 749–755 (2010)
56. A. Afzal, N. Cioffi, L. Sabbatini, L. Torsi, *Sens. Actuators B Chem.* **171–172**, 25–42 (2012)
57. I.B. Pollack, B.M. Lerner, T.B. Ryerson, *J. Atmos. Chem.* **65**, 111–125 (2011)
58. R.K. Sonker, S.R. Sabhajeet, S. Singh, B.C. Yadav, *Mater. Lett.* **152**, 189–191 (2015)
59. X. Pan, X. Zhao, J. Chen, A. Bermak, Z. Fan, *Sens. Actuators B chem.* **206**, 764–771 (2015)
60. C. Zhang, X. Geng, J. Li, Y. Luo, P. Lu, *Sens. Actuators B chem.* **248**, 886–893 (2017)
61. L. Yu, F. Guo, S. Liu, B. Yang, Y. Jiang, L. Qi, X. Fan, *J. Alloys Compd.* **682**, 352–356 (2016)
62. S. Fan, A.K. Srivastava, V.P. Dravid, *Sens. Actuators B chem.* **144**, 159–163 (2010)
63. S. Bernardini, M.H. Benchekroun, K. Aguir, O. Margeat, J. Ackermann, C. Vidolot-Ackermann, *Sens. Transducers* **222**(6), 1–5 (2018)

Publisher's Note Springer Nature remains neutral with regard to jurisdictional claims in published maps and institutional affiliations.

Terms and Conditions

Springer Nature journal content, brought to you courtesy of Springer Nature Customer Service Center GmbH (“Springer Nature”).

Springer Nature supports a reasonable amount of sharing of research papers by authors, subscribers and authorised users (“Users”), for small-scale personal, non-commercial use provided that all copyright, trade and service marks and other proprietary notices are maintained. By accessing, sharing, receiving or otherwise using the Springer Nature journal content you agree to these terms of use (“Terms”). For these purposes, Springer Nature considers academic use (by researchers and students) to be non-commercial.

These Terms are supplementary and will apply in addition to any applicable website terms and conditions, a relevant site licence or a personal subscription. These Terms will prevail over any conflict or ambiguity with regards to the relevant terms, a site licence or a personal subscription (to the extent of the conflict or ambiguity only). For Creative Commons-licensed articles, the terms of the Creative Commons license used will apply.

We collect and use personal data to provide access to the Springer Nature journal content. We may also use these personal data internally within ResearchGate and Springer Nature and as agreed share it, in an anonymised way, for purposes of tracking, analysis and reporting. We will not otherwise disclose your personal data outside the ResearchGate or the Springer Nature group of companies unless we have your permission as detailed in the Privacy Policy.

While Users may use the Springer Nature journal content for small scale, personal non-commercial use, it is important to note that Users may not:

1. use such content for the purpose of providing other users with access on a regular or large scale basis or as a means to circumvent access control;
2. use such content where to do so would be considered a criminal or statutory offence in any jurisdiction, or gives rise to civil liability, or is otherwise unlawful;
3. falsely or misleadingly imply or suggest endorsement, approval, sponsorship, or association unless explicitly agreed to by Springer Nature in writing;
4. use bots or other automated methods to access the content or redirect messages
5. override any security feature or exclusionary protocol; or
6. share the content in order to create substitute for Springer Nature products or services or a systematic database of Springer Nature journal content.

In line with the restriction against commercial use, Springer Nature does not permit the creation of a product or service that creates revenue, royalties, rent or income from our content or its inclusion as part of a paid for service or for other commercial gain. Springer Nature journal content cannot be used for inter-library loans and librarians may not upload Springer Nature journal content on a large scale into their, or any other, institutional repository.

These terms of use are reviewed regularly and may be amended at any time. Springer Nature is not obligated to publish any information or content on this website and may remove it or features or functionality at our sole discretion, at any time with or without notice. Springer Nature may revoke this licence to you at any time and remove access to any copies of the Springer Nature journal content which have been saved.

To the fullest extent permitted by law, Springer Nature makes no warranties, representations or guarantees to Users, either express or implied with respect to the Springer nature journal content and all parties disclaim and waive any implied warranties or warranties imposed by law, including merchantability or fitness for any particular purpose.

Please note that these rights do not automatically extend to content, data or other material published by Springer Nature that may be licensed from third parties.

If you would like to use or distribute our Springer Nature journal content to a wider audience or on a regular basis or in any other manner not expressly permitted by these Terms, please contact Springer Nature at

onlineservice@springernature.com